The Creation and Evolution of Crystal Mush in the Upper Zone of the Rustenburg Layered Suite, Bushveld Complex, South Africa

Z. Vukmanovic [1]*, M. B. Holness [1], M. J. Stock[1] and R. J. Roberts[2]

[1]Department of Earth Sciences, University of Cambridge, Downing Street, Cambridge CB2 3EQ, UK; [2]Department of Geology, University of Pretoria, Hatfield 0002, South Africa

*Corresponding author. Tel: +441223 333474; E-mail: zv211@cam.ac.uk

ABSTRACT

The Upper Zone of the Rustenburg Layered Suite of the Bushveld Complex contains the world's largest Fe–Ti–V $\pm$ P deposit and formed from the last major injection of magma into the chamber. Quantitative textural analysis of Upper Zone rocks was undertaken to constrain the processes operating during mush formation and solidification, focussing on horizons with the greatest density contrast to isolate the effects of gravitational loading. We examined three magnetitite layers, together with their underlying and overlying anorthosites. The similarity of microstructures in anorthosites above and below the dense magnetitite layers suggests that the rocks were not affected by viscous compaction driven by gravitational loading. The magnetitite cumulate layers formed by crystal accumulation from a mobile crystal slurry dominated by the Fe-rich conjugate of an unmixed immiscible liquid. We suggest a new mechanism of crystal nucleation in deforming crystal-rich systems, driven by undercooling caused by cavitation as grains slide past each other during simple shear. We propose that the super-solidus deformation recorded in these rocks was caused by prolonged regional subsidence of the magma chamber at Upper Zone times.

Key words: anorthosite; magnetitite; Bushveld Complex; crystal mush; cavitation creep; subsolidus deformation; microstructure

INTRODUCTION

The fluid dynamical processes that occur in magma chambers are not well understood. Of particular importance is the physical behaviour of the solidifying magma. We still do not have a clear understanding of the mechanisms by which crystal mushes may form, with a variety of possibilities including: *in situ* nucleation and growth in the thermal boundary layers of cooling magma bodies (Hunter, 1996; Namur *et al.*, 2015); crystal settling from a liquid-rich magma body (Woods & Stock, 2019); the accumulation of material derived from the redistribution of crystals grown elsewhere in the chamber (Holness *et al.*, 2017*b*); or by settling from intruding batches of crystal-laden magma (Marsh, 1988; Hunter, 1996; Namur *et al.*, 2015). The subsequent behaviour of such crystal mushes is also poorly constrained, in particular the extent to which gravitational loading results in expulsion of interstitial liquid. Such compaction affects the extent of fractionation in the bulk magma and has been invoked to explain the genesis of some magmatic ore deposits (e.g. Mathez *et al.*, 1997; Boudreau & Meurer, 1999; Meurer *et al.*, 1999; Barnes & Maier, 2002;) and the accumulation of large volumes of erupted crystal-poor magma necessary to feed volcanic eruptions (e.g. Bachmann & Bergantz, 2004).

Here we report the results of a microstructural study of cumulates from the Bushveld Complex, South Africa, combining electron backscatter diffraction (EBSD) analysis with mineral chemistry to address the extent to which gravitational loading by dense magnetite-rich layers affected their underlying low-density plagioclase-rich footwall. We demonstrate that these cumulates

preserve evidence of super-solidus deformation by dislocation creep: this cannot be attributed to internally-generated gravitational loading and most likely occurred in response to regional-scale events. We present evidence to support the concept of cavitation-driven nucleation in deforming crystal mushes and argue that cumulate microstructures may preserve evidence of whole-scale slumping of crystal-rich mushy layers.

GEOLOGICAL BACKGROUND

The Bushveld Complex

The Bushveld Complex was emplaced at 2·06 Ga into sedimentary host rocks of the Transvaal Supergroup, with its floor at ~12 km depth (Buick *et al.*, 2001; Zeh *et al.*, 2015), though some studies suggest that the floor might have been shallower at ~1–3 km (Wallmach *et al.*, 1985). The Bushveld Complex comprises the mafic rocks of the Rustenburg Layered Suite (forming the largest layered intrusion on Earth, Fig. 1) which are capped by the Rooiberg volcanic suite, the Rashoop granophyres and the *c*.4000 m thick Lebowa Granite (South African Committee for Stratigraphy & Geological Survey (South Africa), 1980). The mafic magmas of the Bushveld Complex are thought to have been emplaced during regional extension (Carr &

Groves, 1994). Extension-related subsidence was amplified by loading by the dense mafic magma, resulting in syn-magmatic deformation that continued into the subsolidus (Carr & Groves, 1994; Holness *et al.*, 2017*a*).

The Rustenburg Layered Suite is subdivided into five major zones (Fig. 1): the Marginal, Lower, Critical, Main and Upper Zones (Hall, 1932). The Marginal Zone forms the base of the complex and is dominated by heterogeneous noritic rocks (Engelbrecht, 1985; Wilson, 2012, 2015). The Lower Zone (LZ) is mainly composed of cyclic units comprising dunite, orthopyroxenite and harzburgite (Wilson, 2015). The Critical Zone (CZ) has been sub-divided into the pyroxenitic Lower Critical Zone and noritic Upper Critical Zone, both of which include major chromitite layers (Cameron, 1976; Eales & Cawthorn, 1996). Similarly, the chromite-free Main Zone (MZ) is sub-divided into the norite-dominated Lower Main Zone and gabbronorite-dominated Upper Main Zone. The two are locally separated in the Western Limb by a metre-thick pyroxenite layer (the Pyroxenite Marker), and are considered to have crystallized from a hybrid melt during magma chamber replenishment (Von Gruenewaldt, 1973; Cawthorn *et al.*, 1991*a*; Mitchell, 1996; VanTongeren & Mathez, 2013). The Upper Zone (UZ) has been divided into three sub-zones based on the primocryst assemblage (Von Gruenewaldt, 1973; Tegner *et al.*, 2006): UZa contains cumulus magnetitite;
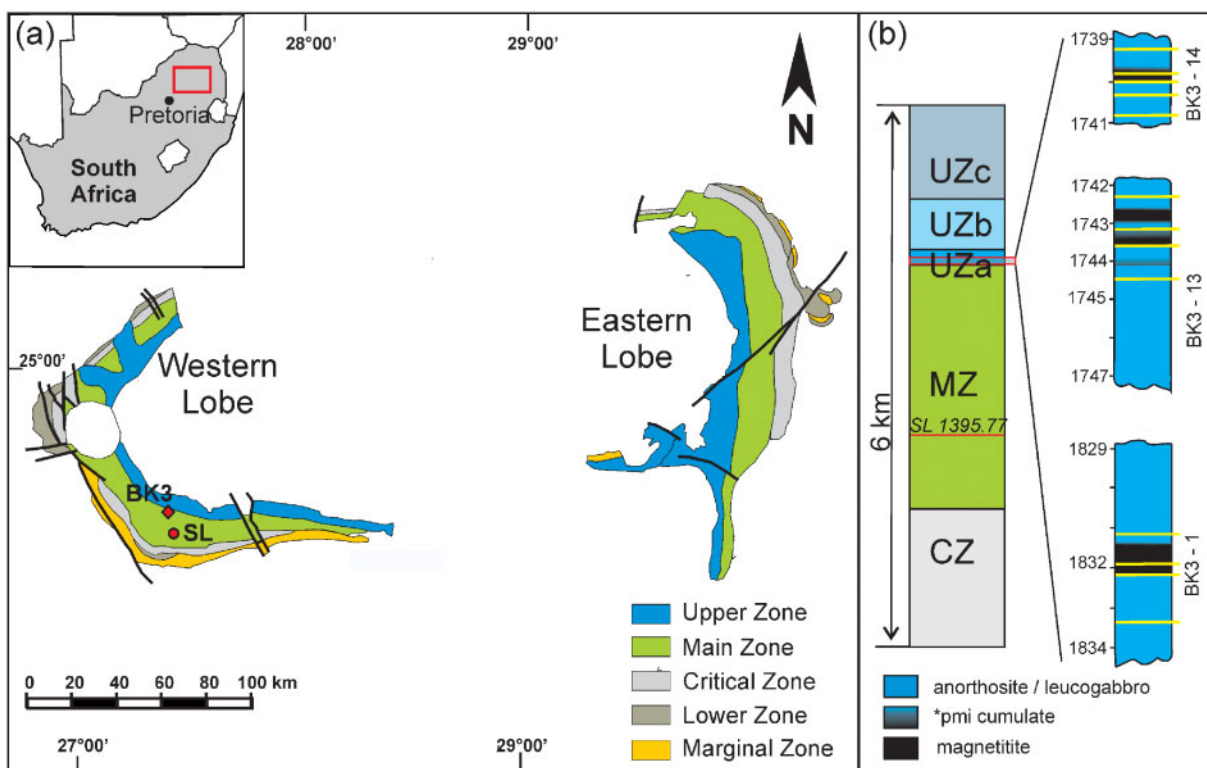
Fig. 1. (a) A simplified geological map of the Rustenburg Layered Suite of the Bushveld Complex. (b) Schematic stratigraphy through the Rustenburg Layered Suite (after Pebane & Latypov, 2017), showing the location of the MZ sample SL12-1395.77, together with a sketch of the parts of the BK3 core used in this study. The abbreviation pmi denotes a plagioclase–magnetite–ilmenite cumulate. Depths in the core are shown in metres, with the suffix of the labels on the right of the core log showing the number of the magnetitite layer (numbers increase upwards stratigraphically). The positions of the samples studied by EBSD are shown by the yellow lines. See Supplementary Data Table S2 for the stratigraphic location of all BK3 samples examined for this study.

UZb additionally contains cumulus olivine; and the appearance of apatite defines UZc. UZa and UZb are dominated by magnetite gabbronorite ($\pm$ olivine), whereas UZc comprises magnetite gabbros, magnetite troctolite and ferrodiorite, together with near-monomineralic magnetite layers and anorthosites. The UZ includes about 30 distinct magnetitite and nelsonite layers (Cawthorn & Molyneux, 1986; Von Gruenewaldt, 1993; Lee *et al.*, 1996; Cawthorn *et al.*, 2005). Apatite-hosted melt inclusions, trace element geochemistry and mass balance calculations have been used to argue for a significant role of liquid immiscibility in the differentiation of UZ (VanTongeren & Mathez, 2012; Fischer *et al.*, 2016; Yuan *et al.*, 2017).

Together with the Upper Main Zone, the UZ is thought to have formed from the last major melt injection in the Bushveld magma chamber (Cawthorn *et al.*, 1991*b*; VanTongeren & Mathez, 2013). The upward mineralogical and chemical evolution in this part of the stratigraphy has been interpreted as a product of closed-system fractional crystallization (Wager & Brown, 1968; Kruger *et al.*, 1987; Tegner *et al.*, 2006; VanTongeren *et al.*, 2010). However, detailed examination of single borehole cores has shown reversals in mineral compositions and density in the UZ, which have been argued to result from replenishment by either primitive melts (Ashwal *et al.*, 2005) or plagioclase-laden magmas (Yuan *et al.*, 2017). Additionally, a regional examination of 5 boreholes showed variable mineralogy and chemistry along strike, which is inconsistent with closed-system fractionation (Scoon & Mitchell, 2012).

The world-class deposits of platinum group elements, vanadium and chromium in the Bushveld Complex have provided the impetus for extensive research over the last century (see Cawthorn (2015) for a review). However, the majority of this research is focussed on geochemistry, with little corresponding work on microstructures (e.g. Boorman *et al.*, 2004; Williams *et al.*, 2006; Vukmanovic *et al.*, 2013; Holness *et al.*, 2017*a*; Kaufmann *et al.*, 2018). The existing microstructural work demonstrates ample evidence for dislocation creep (Vukmanovic *et al.*, 2013; Holness *et al.*, 2017*a*), with undeformed interstitial quartz in rocks containing strongly deformed plagioclase primocrysts attesting to the syn-magmatic nature of this deformation (Holness *et al.*, 2017*a*).

Plagioclase microstructures formed during deformation

In this contribution, we rely on quantitative microstructural interpretations in order to understand the behaviour of the crystal mush in the UZ chamber and its sub-solidus history. We focus particularly on plagioclase deformation microstructures, which are well understood (e.g. Rybacki & Dresen, 2004). Dislocation creep of plagioclase at high temperatures is most commonly achieved by slip on (010)[001] and (001)[110],

with partial recovery leading to the creation of low angle boundaries (Passchier & Trouw, 2005). Whether a boundary represents a twist or a tilt in the crystal structure can be determined by analysis of the misorientation across it, which, for a tilt boundary, is a function of the slip system responsible (see the Supplementary Data; supplementary data are available for downloading at http://www.petrology.oxfordjournals.org for the method of determining slip systems).

The three main mechanisms involved in dynamic recrystallization of plagioclase undergoing dislocation creep are bulging recrystallization (BLG), subgrain rotation (SGR) and high-temperature grain boundary migration recrystallization (GBM) (Gerald & Stünitz, 1993). Which of these mechanisms is dominant can be used to constrain the conditions of deformation (Passchier & Trouw, 2005). BLG and SGR are generally associated with deformation at lower temperatures than GBM and may operate in the subsolidus, whereas GBM may be associated with higher strain regimes (e.g. during regional deformation). Both SGR and, at lower temperatures, BLG, create neoblasts that are crystallographically closely related to their parent. GBM recrystallization is harder to recognise (Drury & Urai, 1990; Ji & Mainprice, 1990; Kruse *et al.*, 2001), but is usually associated with the formation of serrated grain boundaries and strain-free grains (Ji & Mainprice, 1990). In the absence of melt or fluid, neoblast compositions will be indistinguishable from their parent grains, but if melt or fluid were present at the time of deformation, the two grain populations may be chemically distinct (Rosenberg & Stünitz, 2003).

Chemical disequilibrium is known to significantly contribute to, or even drive, feldspar recrystallization (Vernon, 1975; White, 1975; Stünitz, 1998; Rosenberg & Stünitz, 2003). In the presence of melt and at temperatures >850 °C, recrystallization by grain boundary migration is driven by internal strain energy related to differences in chemical potential (Lafrance *et al.*, 1996, 1998; Rosenberg & Stünitz, 2003). Microstructures resulting from this process are characterised by strain-free grains separated by lobate grain boundaries and residual grains (Passchier & Trouw, 2005).

METHODOLOGY

Electron backscatter diffraction analysis

Samples were prepared using the EBSD preparation routine described by Prior *et al.* (1999). Most EBSD analyses were performed using an FEI sFEG XL30 SEM in the Department of Physics, University of Cambridge, and one sample was analysed at the School of Environmental Sciences at the University of Liverpool. Collection of electron backscatter diffraction patterns (EBSDPs) was undertaken using AZtecHKL 2·2 acquisition software. EBSD maps and pole figures were constructed using the Oxford Channel 5 software and the MTex MatLab toolbox (Hielscher & Schaeben, 2008).

For details of acquisition parameters see the Supplementary Data Table S1.

Pole figures were constructed using a lower hemisphere, equal area projection. The fabric strength and type were determined by calculating the J-index, pole figure J-indices (PfJ), M-index and BA-index of the orientation distribution function (ODF) using the MTex MatLab toolbox. We calculated the J- and M-index using the de la Vallée Pousin kernel, and a half-width of 10°, which corresponds to a series expansion of 28. The J–index has a value of one for a random distribution and a value of infinity for a single crystal (Wenk *et al.*, 1998). While the J-index can be used to assess the overall fabric strength, pole figure J-indices (PfJ) describe the characteristics of an individual pole figure. The value of the M-index increases with the strength of the fabric from 0 (random fabric) to 1 (single crystal) (Skemer *et al.*, 2005). We also calculated the BA index which ranges from 0 to 1. The meaning of the BA index is illustrated by values for the three plagioclase fabric types defined by Satsukawa *et al.* (2013): an axial A fabric is defined by a strong point maximum concentration of [100] with parallel girdle distributions of (010) and (001); axial B is defined by a strong point alignment of (010) with a girdle distribution of [100]; and type P is defined by point maxima of [100], (010) and (001). The axial A fabric is associated with high values of BA index (>0·7), an axial B fabric is characterised by a low value of BA index (≈0·2), and the P-type fabric has intermediate values. Axial B fabrics are characteristic of magmatic processes (e.g. crystal settling), type P fabrics are formed as a result of deformation or magmatic flow, whereas axial A fabrics form by deformation.

Electron microprobe

Plagioclase was analysed using a 5WDS Cameca SX-100 Electron Microprobe in the Department of Earth Sciences, University of Cambridge. All major and trace elements were analysed with a 15 kV, 10 nA, defocussed (5 μm diameter) beam. Peak counting times were 10 s for major elements (Si, Al, Na, K, Ca), 60 s for minor (Fe, Mg), and 90 s for trace elements (Ti), with Si and Na analysed first to mitigate the effects of electron beam-induced sample damage. All EPMA data and associated representative uncertainties are given in the Supplementary Data Table S1.

SAMPLES

We chose our sample suite to enable us to focus on the drivers for deformation. We examined a leucogabbro from the lower MZ, previously described by Holness *et al.* (2017a). In the borehole-core SL12 (drilled by Lonplats Mining Company at Mooinooi in the Western Limb; Fig. 1), the base of the Giant Mottled Anorthosite (a marker used to designate the base of the MZ) occurs at a depth of 1546·45 m The borehole-core is dominated by plagioclase-rich norite and is notable for the abrupt

appearance of evidence for significant dislocation creep at around 1540 m depth, and the gradual reduction in the intensity of deformation above ∼1300 m depth: rocks above ∼1000 m are apparently undeformed. We examined an MZ sample from 1395·77 m depth in borehole-core SL12, within the most strongly deformed part of the stratigraphy. Although clinopyroxene first appears in the liquidus assemblage in the strongly deformed region (stratigraphically below our sample), there is no major change in the modal mineralogy (and, therefore, mush density) associated with the onset or cessation of deformation and, critically, the mushy layer was only a few metres thick (Holness *et al.*, 2017a): our chosen MZ sample, therefore, provides an example of deformation that cannot be attributed to gravitationally-driven compaction.

Since the mushy layer through much of the Bushveld stratigraphy was only a few metres thick (Holness *et al.*, 2017a), any effects of compaction must have been on only a local (metric) scale: therefore, to focus on identifying the microstructural record of compaction, we chose a suite of samples in which the density of the crystal mush changes significantly over length scales of a few metres. The many magnetitite layers in plagioclase-rich regions of the UZ present the ideal opportunity to constrain the role of compaction as they result in the greatest possible loading on underlying plagioclase-rich cumulates.

We chose 54 samples from the UZ, focussing on magnetitite layers and their plagioclase-rich footwall and hanging-wall. We sampled the Bierkraal borehole BK3, drilled in the western limb of the RLS (Fig. 1) in a region of stratigraphy containing multiple magnetitite layers (21 in total). These cores have been extensively described by Yuan *et al.* (2017). The sample suite includes three magnetitite layers ranging in thickness from 25 to 113 cm (Supplementary Data Table S2), together with the plagioclase-rich cumulates (either anorthosite or leucogabbro) from both ∼25–50 cm above and ∼10–150 cm below the magnetite layer (Table 1; Supplementary Data Table S2). A sub-set of 14 samples from this suite was analysed by EBSD, including one sample from the each of the three magnetitite layers; a sample of the lower contacts of each of the three magnetitite layers; five samples of footwall; and three samples of hanging-wall (Fig. 1). The thickest magnetitite layer (BK3-13, 113 cm thick) contains a thin (∼10cm) horizon of leucogabbro (Fig. 1b), but can be considered to have acted as a single layer during any gravitationally-driven compaction, since the mush thickness was of the order several metres (Holness *et al.*, 2017a). The lower contacts of the magnetitite layers are generally sharp at the outcrop scale, but the upper contacts are commonly gradational over tens of centimetres (Supplementary Data Table S2). The mineral modes of all examined samples are shown in Table 1. Plagioclase compositions were determined in a suite of samples associated with one of the three magnetitite layers, including three footwall samples, one

Table 1: Plagioclase grain shape and mineral mode of MZ and UZ samples. The average apparent aspect ratio, AR, of plagioclase is calculated based on a perfect fit of an ellipsoid, and two values are given: one for small grains and the other for large grains. The minimum number of grains used to calculate AR (for large grains in sample BK3-13–12) is 70: all other values of AR are based on populations of more than 100 grains. Mineral modes were obtained using point counting

zone	sample	depth in core (m)	layer	AR		mineral mode (vol.%)				
				large	small	Pl	Mt	Il	Px	Ol/Qtz
MZ	SL12-1395.77	1395·77	A			90			5	5
UZ	BK3-1-2	1833·35	underlying A	1·8	1·43	87·89	9·01	2·01	1·09	
	BK3-1-9b	1832·11	contact			31·87	59·92	2·58	4·30	1·30
	BK3-1-11	1831·91	magnetitite	2·53	1·3	32·91	63·16	3·93		
	BK3-1-15	1831·17	overlying A	1·98	1·41	87·94	11·07	0·99		
	BK3-13-1	1744·58	underlying LG	2·19	1·35	75·34	10·91	1·72	12·03	
	BK3-13-5b	1743·61	contact			70·12	4·76	0·05	25·08	
	BK3-13-8a	1743·17	pmi			48·11	49·76	2·12		
	BK3-13-12	1742·3	overlying A	2·42	1·47	81·35	17·92	0·73		
	BK3-14-2	1740·82	underlying LG	2·17	1·41	81·12	6·12	0·87	11·89	
	BK3-14-4	1740·36	underlying LG	2·4	1·41	86·12	10·23	0·68	2·97	
	BK3-14-7d	1739·96	contact			51·18	44·70	0·38	3·74	
	BK3-14-8a	1739·81	magnetitite			52·76	44·49	2·75		
	BK3-14-10a	1739·23	overlying A	2·05	1·43	72·31	26·76	0·94		

Abbreviations: A, anorthosite; LG, leucogabbro; pmi, plagioclase–magnetite–ilmenite cumulate (pmi nomenclature following Irvine 1982; Yuan *et al.*, 2017). Pl, plagioclase; Mt, magnetite; Il, ilmenite; Px, pyroxenes; Ol, olivine; Qtz, quartz. Values for Ol/Qtz in SL12-1395.77 are referring to Qtz %. Values for Ol/Qrtz in BK3-1–9 are referring to Ol %.

hanging-wall sample, two samples from the lower contact, and one from the magnetitite layer itself (Supplementary Data Table S3). None of the samples were oriented, although the direction of the paleovertical orientation is known relative to the drillcore.

PETROGRAPHY

Main Zone
The MZ leucogabbro is characterised by large (apparent size: ~2500 μm long axis) plagioclase grains that define a strong fabric. These large crystals commonly show evidence of lattice distortion (Fig. 2a) and stepped and irregular grain boundaries. They are typically surrounded by abundant smaller plagioclase grains < 500 μm across (Fig. 2b–d). The large plagioclase crystals show evidence of lattice distortion at their margins (Fig. 2c) adjacent to the fine plagioclase grains (Fig. 2d). Other cumulus phases, such as pyroxene and interstitial quartz, are undeformed (Fig. 2a, b).

Upper Zone
Plagioclase-rich cumulates
The anorthosites or leucogabbros stratigraphically above and below the magnetite layers are characterised by bimodal plagioclase grain size distributions (Fig. 3a–d; Fig. 4d–f). The larger crystals (apparent size: >1000μm long axis) are euhedral to subhedral and appear elongate in thin section, with an average apparent aspect ratio between 1·8 and 2·4 (Table 1). The euhedral large grains have straight grain boundaries parallel to the growth faces but are often stepped on a small scale (Fig. 3a, c, d). Some subhedral large grains show slightly serrated grain boundaries (Fig. 3b, Fig. 4e black dotted line). The larger crystals contain deformation twins

(Fig. 3), low angle boundaries (Fig. 3d) and often show undulatory extinction (Figs 3b, d; Figs 4b, e). In contrast, the smaller grains (apparent size: <1000 μm long axis) are equant (average apparent aspect ratio of ~1·4, Table 1), and preserve less evidence of intra-grain deformation (Figs 3a–d, 4d, e). These smaller grains are generally distributed along the grain boundaries of larger grains (Figs 4d, e). The smaller grains commonly contain growth twins, but deformation twins are also present (Figs 3a, c). The thin leucogabbro horizon within the thick magnetitite layer BK3-13 does not show any observable differences to those above and below the magnetitites.

In leucogabbros, clinopyroxene is typically interstitial (Fig. 3d) and generally contains orthopyroxene exsolution lamellae (Fig. 4f). A few pyroxene crystals show undulatory extinction or rare low angle boundaries. Despite being part of the primocryst assemblage, interstitial overgrowth on oxides resulted in a subhedral habit (Fig. 3c). Rare interstitial quartz (<100 μm) is present and appears strain-free (Fig. 3f). Reactive symplectites composed of plagioclase and augite are common in both anorthosites and leucogabbros, replacing plagioclase primocrysts and commonly spatially associated with undeformed, euhedral biotite (Fig. 3e, f). Following Holness *et al.* (2010), we interpret them as a product of reaction between an iron-rich immiscible conjugate liquid and the surrounding primocrysts, following the loss of the Si-rich conjugate.

Magnetitite layers
Magnetitite layers contain ~60 vol. % magnetite, with subsidiary plagioclase (~30–35 vol. %) and ilmenite (5–10 vol. %). On a thin section scale, the apparently sharp lower contact is revealed to be highly undulatory, with
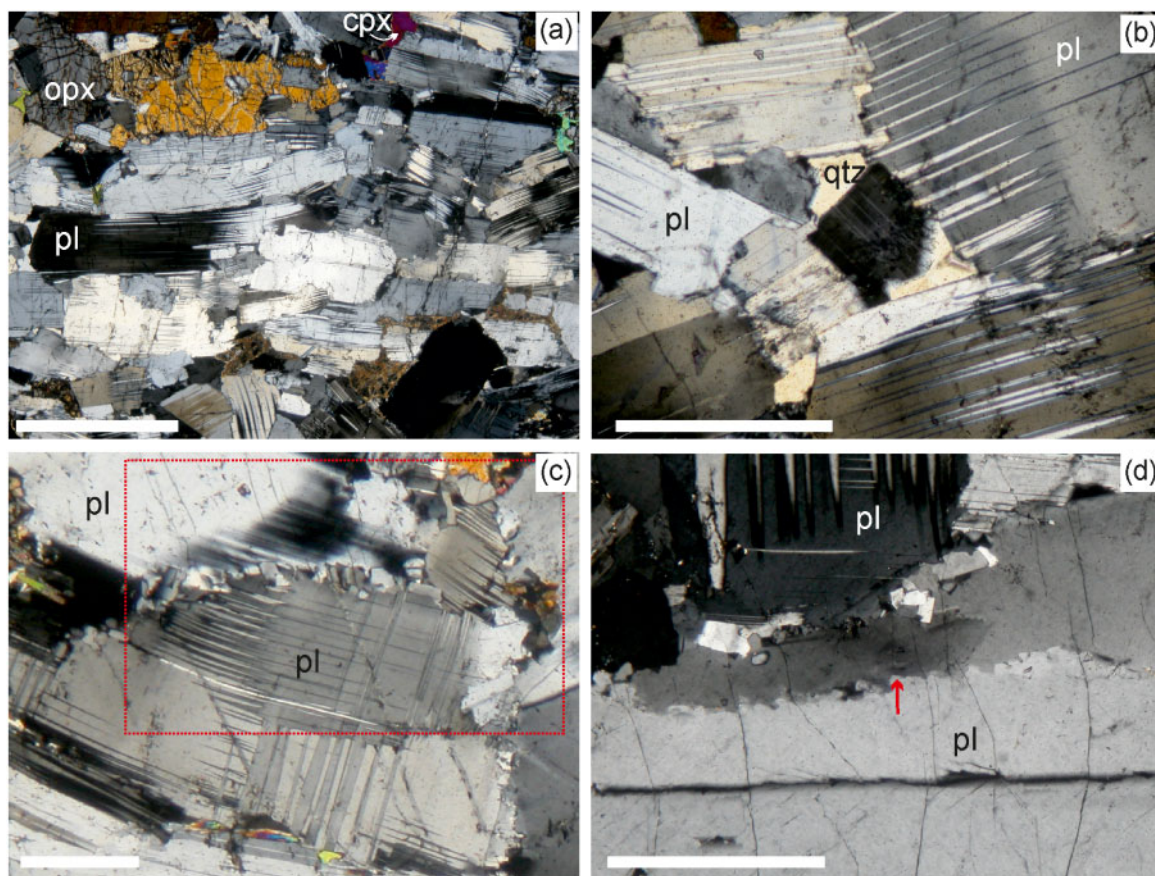
Fig. 2. Photomicrographs of the plagioclase-rich sample (SL12-1395.77) from the Upper Main Zone. (a) A general view showing bent plagioclase (pl), primocrystic orthopyroxene (opx) and interstitial clinopyroxene (cpx). Scale bar: 2 mm. (b) Undeformed interstitial quartz (qtz) fills the space between plagioclase primocrysts. Plagioclase crystals contain discontinuous (deformation) twins. Scale bar: 2 mm. (c) Fine-grained plagioclase crystals along the boundaries of two larger plagioclase grains. The crystallographic orientations of grains in the region outlined by the red box are shown in Fig. 6. Scale bar: 2 mm. (d) Evidence for grain boundary bulging (red arrow) in large plagioclase crystal. Scale bar: 2 mm.

mm-scale extension of oxides into the silicate footwall, outlined by abundant fine polycrystalline olivine (Fig. 4a).

Plagioclase within the oxide layer is commonly aligned, forming a foliation (Fig. 4b). It is generally separated from the surrounding oxide by a thin film of polycrystalline biotite or olivine, and/or is partially replaced by reactive symplectites (Fig. 4b, c). Some plagioclase grains appear entirely recrystallized to form aggregates of randomly oriented grains that preserve the elongated shape of the original grain (Fig. 4b, c), such recrystallization is best developed where several of the original large grains are in close proximity (Fig. 4c). While most plagioclase grains within magnetitite layers are elongated tabular crystals or part of a recrystallized cluster (replacing either single isolated laths or clusters of original laths), some are much smaller and form isolated rounded grains (Fig. 4c). Magnetite grain size inversely correlates with plagioclase mode, with relatively fine-grained magnetite ($<500\,\mu m$ in diameter, compared to the usual $5000\,\mu m$ diameter) in samples with >20 vol. % plagioclase (Supplementary Data Fig. S1).

QUANTIFICATION OF PLAGIOCLASE FABRICS

Main Zone

The foliation defined by larger plagioclase crystals in the MZ leucogabbro is parallel to the floor of the magma chamber (Fig. 5) and is defined by a preferred grain orientation with [100] and (010) planes parallel, and (001) perpendicular to the foliation (Fig. 5). The relationship between the (010) and (001) planes attests to a predominantly tabular plagioclase grain shape (Morales *et al.*, 2011, Holness *et al.*, 2017*b*). A preferred orientation of the small plagioclase crystals ($<800\,\mu m$) defines the same crystallographic fabric (Fig. 5b). In both cases, the fabric BA index (e.g. 0.17, Table 2) attests to its magmatic origin. The misorientation axes are parallel to foliation and correspond to the [100] axis (Fig. 5b).

The small plagioclase grains that surround the larger grains form groups with a very similar crystallographic orientation, but with an angular difference of $\sim 40°$ compared to the adjacent large grain (Figs 2c, 6). The large grains commonly show evidence for lattice distortion ($\sim 15–20°$) and contain low angle boundaries, as well as subgrains (Supplementary Data Fig. S2). Of the 15 low
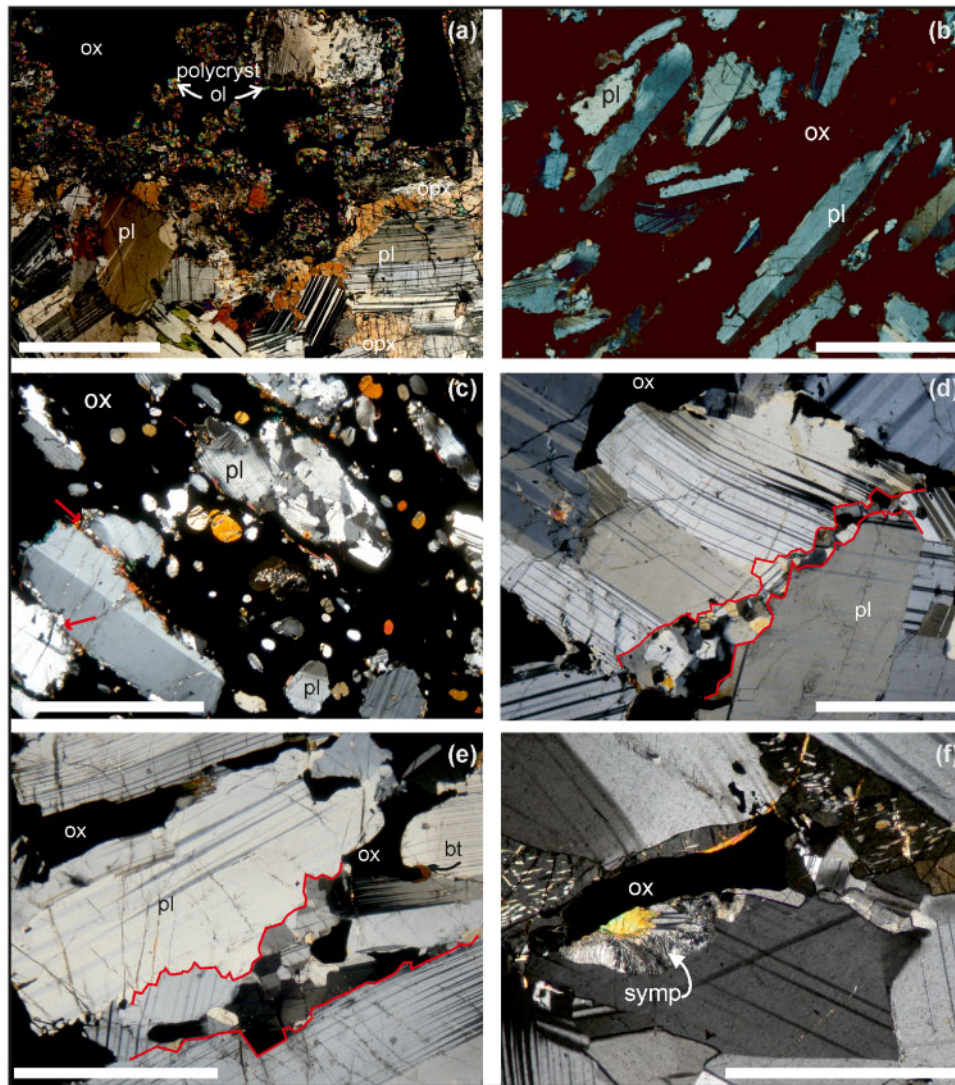
Fig. 3. Photomicrographs of the anorthosite cumulates underlying magnetitite layers. (a) Fine-grained plagioclase crystals distributed between large plagioclase crystals. Red line indicates stepped grain boundaries of the large grains. (b) Large anhedral plagioclase with stepped grain boundaries (blue arrow) is surrounded on one side with small, apparently randomly orientated, plagioclase crystals (red arrow), and on the opposite side with euhedral crystals with parallel grain boundaries. (c) Small plagioclase grains distributed between two large plagioclase crystals. The small plagioclase crystals show some undulatory extinction, whereas the large crystals contain wedged (deformation) twins. Red lines highlight the location of small plagioclase crystals between large crystals. (d) Interstitial clinopyroxene between plagioclase grains. Note that plagioclase has curved boundaries even when in contact with another phase (i.e. clinopyroxene); (blue arrow). (e) Reactive symplectite and biotite on plagioclase grain boundaries. (f) Undeformed interstitial quartz is present within the pore space of plagioclase cumulate. Abbreviations: pl, plagioclase; cpx, clinopyroxene; symp, symplectite; bt, biotite; ox, magnetite. Scale bars: 1 mm.

angle boundaries analysed in this sample, more than half are tilt boundaries created by slip on (010)[001].

Upper Zone
The orientation of the plagioclase crystals in the UZ samples that we examined partly correlates with their grain size (Figs 7a, b). The orientation of large (>1000 μm) and small (<1000 μm) grains is almost identical (Fig. 7c, f), with [100] and poles to the (010) plane parallel to foliation, whereas poles to the (001) plane are randomly distributed (Fig. 7c, d). The relationship between the (010) and (001) planes attests to a predominantly tabular grain shape (Morales *et al.*, 2011; Holness *et al.*, 2017*b*). However, both M- and J-indices show that the fabric defined by the larger grains is stronger than that defined by the smaller grains (see Supplementary Data Figs S3, S4). The BA index is within the range 0·17 to 0·64 (Table 2). Our UZ samples record three types of fabric: P, axial B and axial A (Satsukawa *et al.*, 2013). Most samples record a P-type fabric (e.g. defined by point maxima for all three axes), indicative of crystal lineation (Table 2, Supplementary Data Figs S3, S4). This is most strongly defined by the smaller grains. In other samples, the second most abundant fabric is axial B-type (e.g. a foliation defined by

Fig. 4. (a) Photomicrograph of the contact between underlying anorthosite and overlying magnetitite layer. Polycrystalline olivine is present along the contact. (b)–(c) Photomicrographs of the magnetitite layer. (b) Aligned plagioclase crystals within the magnetitite layer. (c) Within the magnetite layer are numerous isolated rounded grains and polycrystalline aggregates of plagioclase. The polycrystalline aggregates are likely to be the result of complete recrystallization of original single grains, since many of the remaining large single grains have recrystallized margins (red arrows). Fine-grained biotite and reactive symplectites are present along boundaries between plagioclase and magnetite grains. (d)–(f) Photomicrographs of anorthosites overlying the magnetitite layers. (d) Fine-grained plagioclase present along the grain boundaries of large plagioclase. (e) Irregular boundary separating large plagioclase crystals. (f) Plagioclase–clinopyroxene symplectites along the plagioclase–magnetite grain boundary, replacing the plagioclase primocrysts. Red lines highlight the location of small plagioclase crystals between large crystals. Abbreviations: pl, plagioclase; ox, magnetite; polycryst ol, polycrystalline olivine; opx, orthopyroxene; bt, biotite; symp, symplectite. Scale bars: 1 mm.

alignment of (010) planes), which is typical of undeformed layered intrusions (e.g. Holness *et al.*, 2017*b*) and ophiolites (Morales *et al.*, 2011; Satsukawa *et al.*, 2013; VanTongeren *et al.*, 2015). This fabric is most strongly defined by large grains (Table 2, Fig. 7, Supplementary Data Figs S3, S4). Axial B and P-type fabrics are not systematically confined to either hanging wall or footwall layers (Table 2). A small number of samples, mainly those dominated by magnetite, contain plagioclase with an axial A-type fabric, characteristic of deformation (Table 2, Supplementary Data Figs S3, S4). Misorientation axes for the bulk samples (i.e.

for both grain size populations) show that misorientation axes coincide with [100] axes (i.e. in the same plane as the foliation; Fig. 7c, f).

The most common microstructure shows no crystallographic relationship between neighbouring plagioclase grains of different size (Fig. 8a, b). The pole figures of the larger grains generally show unambiguous evidence for crystal deformation, with strong dispersion of the orientation of (010) and (001) around the [100] axis (Fig. 8b). The nearby small grains are either only weakly deformed or undeformed, with clustered orientations of the [100] axis and (010) planes (Fig. 8b).
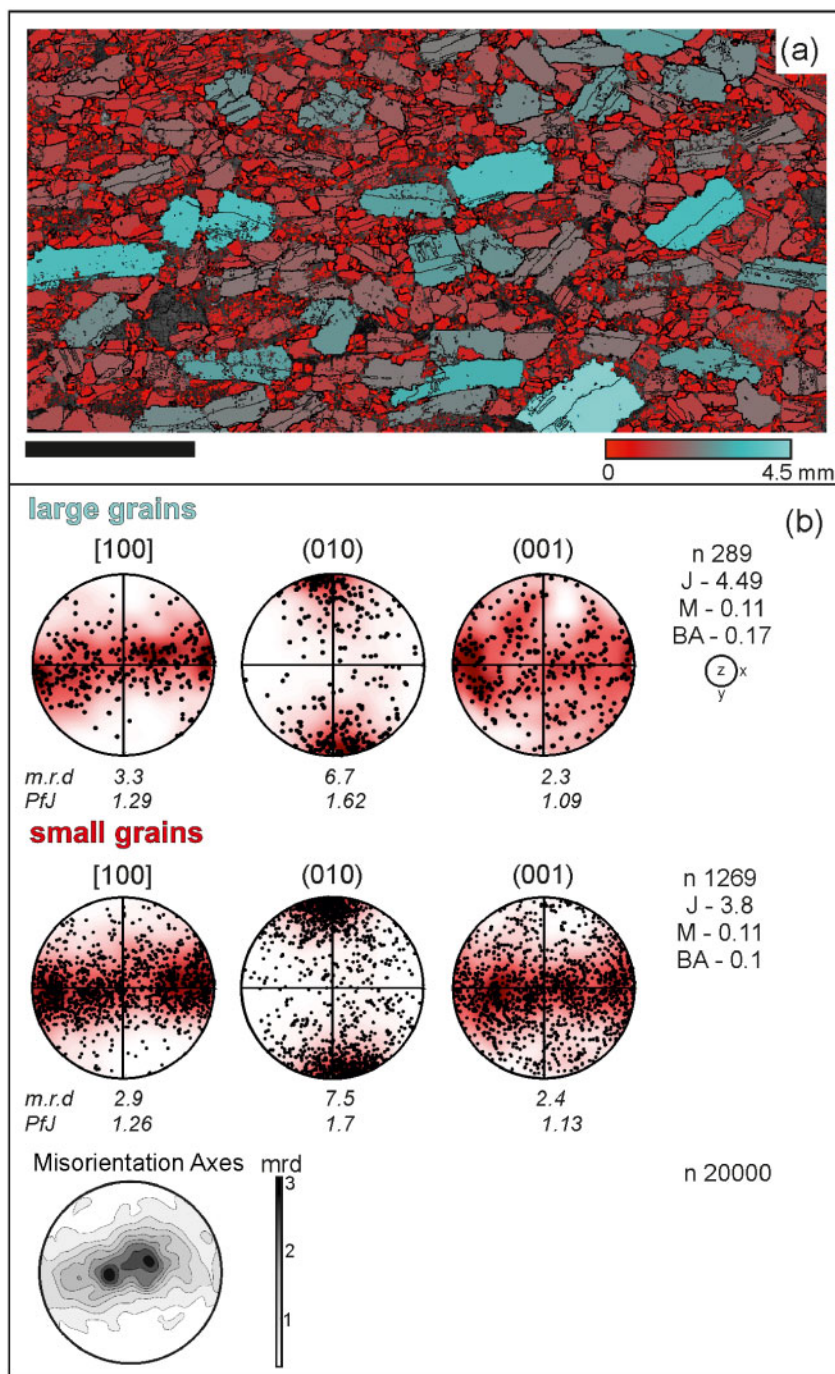
Fig. 5. (a) Plagioclase EBSD grain size map of the SL12-1395.77 MZ sample. The map is constructed using an equivalent circle diameter (ECD) of plagioclase grains. Rock foliation is parallel to the X direction of the map (Y is the pole to foliation) (b) Pole figures for the large plagioclase grains (>1000 μm ECD), small plagioclase grains (<1000 μm ECD) and density contour diagram of plagioclase misorientation axes. Abbreviations: mrd, multiples of a random distribution; PfJ, J- index of individual pole figures; n, number of grains; J, J-index; M, M-index; BA, BA- index.

The few small grains in clusters have a close orientation to the neighbouring large grains (Fig. 8c, Supplementary Data Fig. S5). In rare cases, we observe very similar crystallographic orientations in neighbouring grains of different size. An example is shown in Fig. 8c, where a gradual increase in crystallographic misorientation is observed across a low angle boundary associated with a subgrain along the profile A–A'. Dispersion of (010) and (001) occurs around the [100] axis, consistent with operation of the (010)[001] slip system during dislocation creep (Supplementary Data Fig. S6). The smaller crystals were, therefore, produced by either BLG or SGR recrystallization, both of which produce neoblasts with a similar orientation to their parent (Rosenberg & Stünitz, 2003; Passschier & Trouw, 2005; Svahnberg & Piazolo, 2010).

Table 2: CPO characteristics of the anorthosites studied here

sample	layer	grain size	N	BA	J-index	PfJ 100	PfJ 010	PfJ 001	M-index	CPO
SL12-1395.77	A	large	289	0·17	4·49	1·29	1·62	1·09	0·11	B
		small	1269	0·10	3·80	1·26	1·70	1·13	0·11	B
BK3-1-2	underlying A	small	272	0·48	2·47	1·09	1·04	1·04	0·02	P
		large	733	0·31	1·90	1·08	1·06	1·04	0·02	B
BK3-1-9b	contact	large	240	0·50	5·14	1·30	1·32	1·07	0·06	P
		small	183	0·55	5·29	1·32	1·25	1·09	0·06	P
BK3-1-11	magnetitite	large	85	0·25	1·03	1·40	1·37	1·13	0·00	B
		small	237	0·64	4·21	1·21	1·11	1·09	0·03	A
BK3-1-15	overlying A	large	162	0·33	6·54	1·35	1·36	1·11	0·08	B
		small	488	0·35	2·15	1·07	1·08	1·03	0·02	B
BK3-13-1	underlying LG	large	135	0·41	6·91	1·49	1·49	1·15	0·09	P
		small	465	0·43	4·17	1·30	1·33	1·09	0·08	P
BK3-13-5b	contact	large	364	0·14	2·83	1·12	1·12	1·05	0·04	B
		small	535	0·42	2·12	1·09	1·06	1·04	0·02	P
BK3-13-8a	pmi	large	58	0·75	1·03	1·43	1·33	1·24	0·00	A
		small	882	0·49	1·67	1·03	1·04	1·01	0·01	P
BK3-13-12	overlying A	large	209	0·45	3·32	1·16	1·14	1·06	0·03	P
		small	1038	0·57	1·93	1·11	1·06	1·04	0·03	P
BK3-14-2	underlying LG	large	167	0·37	5·21	1·29	1·26	1·08	0·06	B
		small	584	0·38	2·10	1·11	1·08	1·02	0·03	B
BK3-14-4	underlying LG	large	164	0·57	5·93	1·36	1·29	1·13	0·07	P
		small	904	0·44	1·75	1·06	1·05	1·03	0·02	P
BK3-14-7d	contact	large	154	0·37	6·05	1·17	1·20	1·09	0·05	B
		small	284	0·40	2·71	1·07	1·11	1·04	0·03	P
BK3-14-8a	magnetitite	large	272	0·60	2·45	1·08	1·05	1·03	0·02	A
		small	3292	0·50	1·23	1·03	1·01	1·01	0·01	P
BK3-14-10a	overlying A	large	206	0·46	3·36	1·17	1·10	1·06	0·04	P
		small	571	0·43	2·04	1·09	1·03	1·05	0·03	P

N, number of grains measured; BA, index; PfJ, pole figure index for three main axes; type of CPO shown are axial–B, type P and axial–A fabrics (see text for detailed explanation of CPO types). Other abbreviations as in Table 1.

The extent of crystallographic misorientation within large plagioclase crystals can vary from ~10° to >35° (Fig. 8c, Supplementary Data Fig. S4a). Low angle boundaries are often parallel within a single crystal and the predominant slip system is (010)[001]. There is no systematic variation in the amount of crystal plasticity relative to the position of magnetite layers (Supplementary Data Fig. S6a).

Clinopyroxene primocrysts commonly contain low angle boundaries, with lattice distortion of <25°. Interstitial clinopyroxene is generally less deformed than the associated primocrysts, with no low angle boundaries (Supplementary Data Fig. S6b). Both plagioclase and clinopyroxene crystals within the late reactive symplectites show no evidence of crystal plasticity (Fig. 9).

PLAGIOCLASE MICROSTRUCTURE IN THE MAGNETITITE LAYERS

Plagioclase crystals within the magnetitite layers show a different microstructure to those in anorthosites and leucogabbros, falling into four types: (1) isolated round grains (Fig. 4c); (2) isolated, subhedral, elongate, grains that record evidence of minor plastic deformation (~10° of crystal distortion) with only minor marginal recrystallization (Fig. 10a); (3) grains that preserve their original shape but with extensive recrystallization along grain boundaries with other plagioclase grains (Fig. 10b), the

orientation of these neoblasts progressively changes from that of the adjacent larger crystal with increasing distance from the latter; and (4) completely recrystallized grains, comprising neoblasts with no evidence for a retained magmatic CPO (Fig. 10c). The third and fourth categories of grains are most common in plagioclase-rich zones (Fig. 10b, c), suggesting that recrystallization is most common where the original large laths formed clusters.

PLAGIOCLASE MINERAL CHEMISTRY

Plagioclase compositions (core and rim) were measured in large and small grains from six UZ samples (both above, below and within, a magnetitite layer; Supplementary Data Table S3). The plagioclase anorthite number (An# = Ca/(Ca+Na) x 100) varies between 55 and 77 (Fig. 11a) and correlates with grain size (quantified using the Feret diameter). The small crystals (<1000 μm) have An# in the range 55–77 (mean ~60) and include the most primitive (i.e. highest An#) crystals (Fig. 11a). Coarser plagioclase grains (>1000 μm) typically have more evolved compositions (i.e. lower An#) that fall in a narrow range with An# typically 50–62 (mean ~58; Fig. 11a). Individual crystals have homogeneous anorthite contents, with An# varying by <2 between the cores and rims of single large grains (Supplementary Data Table S3).
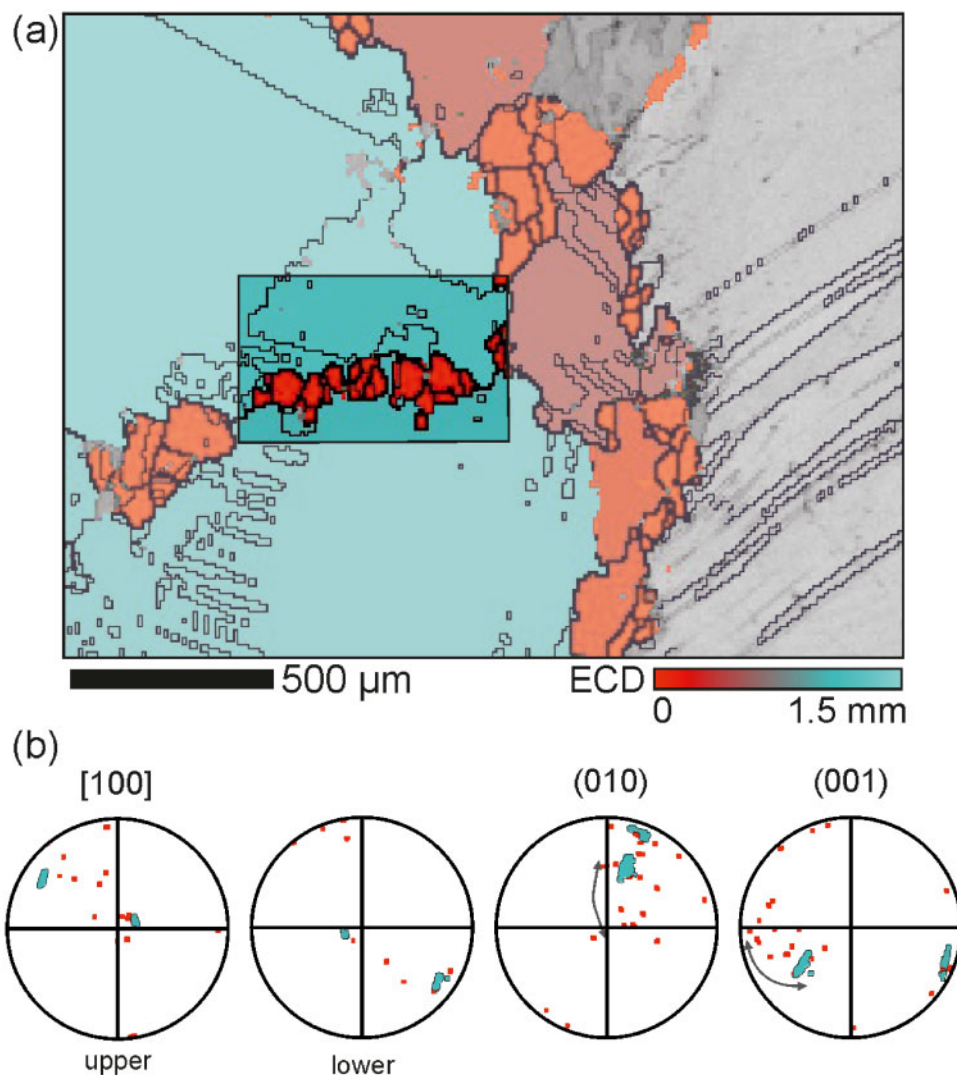
Fig. 6. (a) The grain size EBSD map of the region shown in Fig. 2c. The grain size map is constructed using the ECD of plagioclase grains, with grain size shown as different colours from red (0 mm) to teal (1·5 mm). The inset shows the selected small grains and their neighbouring large grains that are plotted on the pole figures in (b). (b) Pole figures show the crystallographic orientation of the small and two large plagioclase grains. Red arrows show orientation difference between large and small grains (∼40°). The number of points on the pole figures is 2760.

DISCUSSION

Chemical differences between the two populations of plagioclase grains

According to Yuan *et al.* (2017), ilmenite first crystallizes in the UZ when the plagioclase An# is ∼58. Although some grains in our UZ samples have high An# (<77) and likely crystallized before ilmenite joined the liquidus, most of our feldspar measurements have An# within analytical uncertainty of ilmenite saturation (i.e. ∼58; Fig. 11a), consistent with their proximity to the magnetitite layers. The smaller plagioclase grains are often more anorthitic than larger grains, suggesting that they either crystallized from a more primitive liquid or record more extensive reaction with an interstitial (chemically isolated) Fe-rich conjugate liquid (which would contain abundant Ca and P) than the larger grains (e.g. Humphreys, 2011). The latter hypothesis is

supported by the spatial association between small anorthite-rich plagioclase grains and reactive symplectites (Fig. 9d). However, a more detailed study of the plagioclase chemistry (e.g. zoning and precise trace element measurements) is required to fully understand the An# relationship with grain size.

### The cause of plastic deformation in the leucogabbros and anorthosites

Both the MZ leucogabbro and the UZ anorthosites and leucogabbros preserve abundant evidence of deformation by dislocation creep. The misorientation axes in all samples are uniformly parallel to the foliation, suggesting that each of our samples experienced a single deformation event (cf. Reddy & Buchan, 2005; Michels *et al.*, 2015; Vukmanovic *et al.*, 2018*b*). Furthermore, the absence of plastic deformation recorded by interstitial
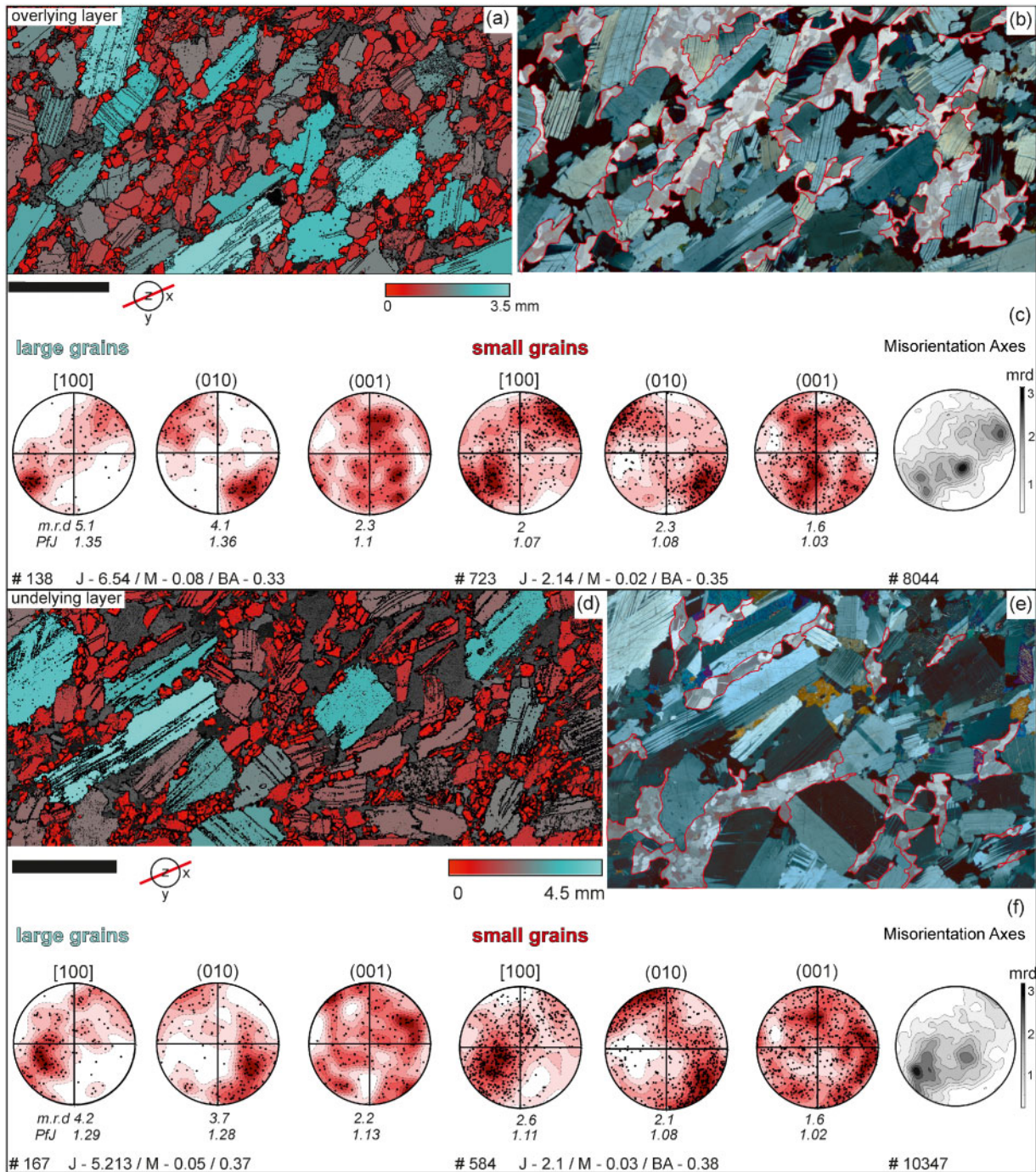
Fig. 7. (a) EBSD grain size map for a plagioclase-rich cumulate layer overlying magnetitite, with the grain sizes ranging from 0–3·5 mm, shown by colours from red to teal. (b) Photomicrograph of the area shown in (a). (c) Pole figures for the large plagioclase grains (>1000 μm ECD), small plagioclase grains (<1000 μm ECD) and density contour diagram of plagioclase misorientation axes. (d) EBSD grain size map for the underlying plagioclase-rich cumulate layer. (e) Photomicrograph showing the area analysed in (d). The red line in a white ellipsoid represents the foliation (24° to horizontal). In both (b) and (e), the distribution of the small plagioclase grains is highlighted by white-red overlay.

quartz and the reactive symplectites, and only weak deformation of interstitial clinopyroxene, suggests that this single deformation episode was confined to the super-solidus, when a significant volume of melt was present in the crystal mush (in agreement with Holness *et al.*, 2017*a*).

Drivers for super-solidus deformation are either internally-generated, such as gravitational loading by the overlying mush (Sparks *et al.*, 1985; Meurer & Boudreau, 1998; McKenzie, 2011; Holness *et al.*, 2017*b*), or externally-generated and related to regional tectonics (Carr & Groves, 1994). We consider it unlikely that
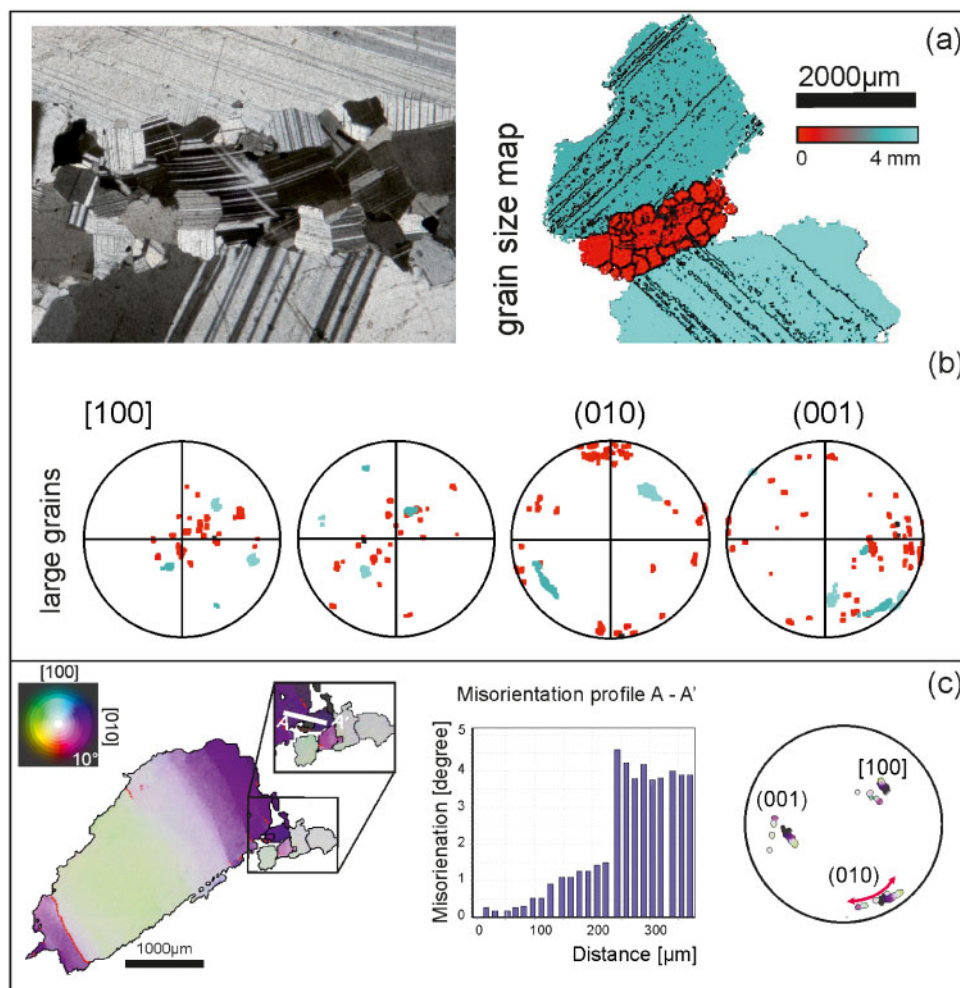
Fig. 8. (a) Photomicrograph and grain size map, using ECD, of two large plagioclase grains and their fine-grained neighbours. (b) Pole figure data for the two large grains (teal) and their fine-grained (red) neighbours. (c) Misorientation map of a large plagioclase grain and two smaller neighbours. The map is coloured using the inverse pole figure (IPF) key referenced to the mean orientation of a grain. The colour scale (top left) is adjusted so that white represents 0° and black represents 10° of misorientation. Misorientation profile A–A' showing an increase of misorientation towards two small neighbouring grains. Pole figure data for the large grain and its neighbours, shows that the dispersion axis (i.e. axis that experienced a minimum of dispersion) is [100], whereas dispersion between the small grains and the large grain is ∼ 20°.

gravitationally-driven compaction was the main cause of the deformation observed in the MZ leucogabbro, because dislocation creep is confined to a particular stratigraphic horizon in the SL12 drill core, with no correlation between the strength of deformation and the modal mineralogy of the crystal mush (Holness *et al.*, 2017*a*).

Our comparison of both the footwall and hanging-wall of the UZ magnetitite layers leads us to the same conclusion. Critically, our results show that the amount of plastic deformation experienced by plagioclase-rich cumulates is the same both above and below magnetitite layers, regardless of the thickness of the magnetitite. Hence, if compaction had occurred it cannot have involved dislocation creep. Furthermore, if the footwall had been affected by viscous compaction by pressure-solution processes we might expect to see smaller modal proportions of interstitial phases compared to the hanging-wall, but this is generally not observed

(Table 1). There is no consistent relationship between fabric strength and stratigraphic position relative to the magnetitite layers; footwall samples may have a weaker fabric than those above (Table 2), inconsistent with the fabrics forming by pressure-solution (c.f. Meurer & Boudreau, 1998).

As our microstructural data are inconsistent with internally-driven deformation by viscous compaction by either dislocation creep or pressure-solution, we instead suggest that the high-temperature deformation recorded by our MZ and UZ leucogabbros and anorthosites is related to external, progressive and long-lasting regional subsidence of the magma chamber (e.g. Carr & Groves, 1994; Maier *et al.*, 2013). Interestingly, the absence of evidence of deformation in grains formed during the last stages of solidification (i.e. the reactive symplectites and the interstitial quartz) suggests that such subsidence only affected the crystal mush while it contained more than a few vol. % liquid.
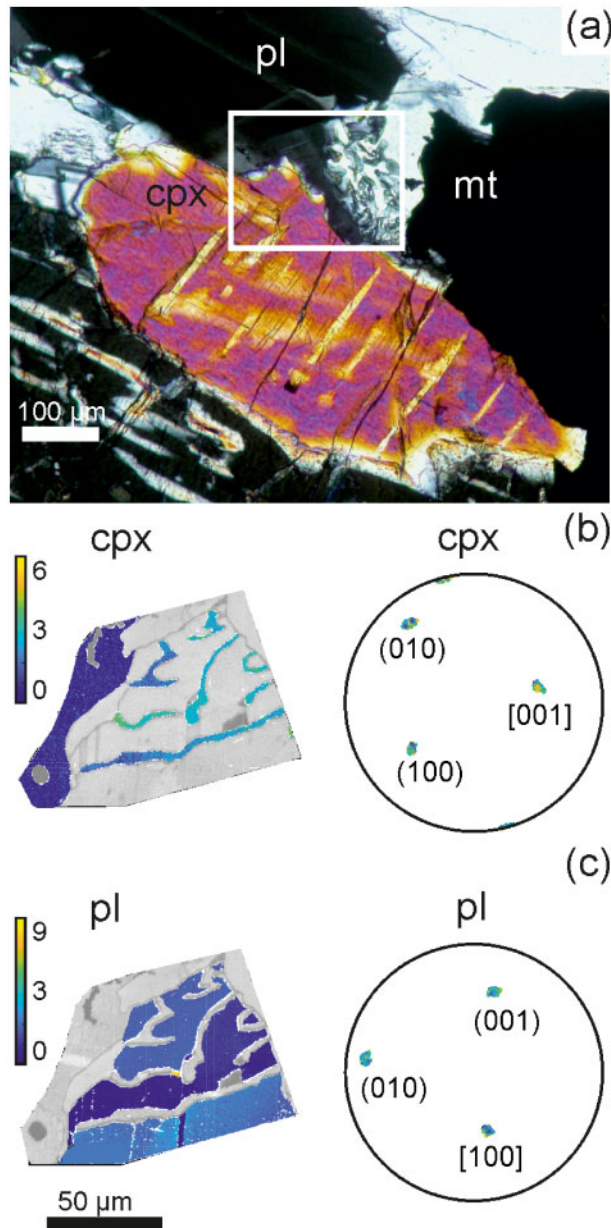
Fig. 9. (a) Photomicrograph of reactive symplectites surrounding clinopyroxene (cpx) and magnetite (mt) and replacing plagioclase (pl). EBSD maps showing average misorientation within clinopyroxene (b) and plagioclase (c) within the symplectite and the corresponding pole figures. The absence of the spread in pole figures confirms the grains comprising the symplectite are undeformed.

The cause of plagioclase deformation in the magnetitite layers

Plagioclase grains in the UZ magnetitite layers experienced a different deformation history to those in the over- and underlying anorthosites and leucogabbros. Of particular importance is the observation that the degree of deformation recorded by each plagioclase grain correlates with the local plagioclase mode. Isolated crystals surrounded by magnetite record only minor lattice distortion (Fig. 10a), whereas nearby groups and clusters of plagioclase grains are either partially or fully

recrystallized (Fig. 4b, c; Fig. 10b, c). The greater extent of deformation for clustered compared to isolated plagioclase grains suggests that the deformation took place in an essentially liquid environment, in which isolated grains were able to move freely while clustered grains experienced local jamming (e.g. Bergantz et al., 2017). In this case, the magnetitite layers must have originally been very liquid-rich, rather than representing crystal accumulations. Such a liquid would necessarily be the Fe-rich immiscible conjugate of a fully-unmixed immiscible magma. This interpretation is consistent with the suggestion of Maier et al. (2013) that the magnetitite layers formed from liquid-rich slurries, containing plagioclase and magnetite grains in an Fe-dominated liquid. It is also consistent with the presence of abundant reactive symplectites that partially replace the plagioclase grains, both within the magnetitite layer and at its base, indicating reaction with an Fe-rich liquid (e.g. Holness et al., 2010). The numerous small, rounded plagioclase grains may have originally formed part of recrystallized laths that subsequently disintegrated during flow of the liquid-rich mush. The generally sharp and planar lower contact of the magnetitite layers is consistent with a generally thin ($\sim$1 m) mushy layer in the Bushveld (Holness et al., 2017a); we envisage these mobile slurries moved across an almost completely solidified plagioclase-rich floor into which interstitial (and reactive) liquid locally percolated only a few centimetres (Fig. 4a).

A new phenomenon: cavitation-driven nucleation?

Microstructures in the MZ leucogabbro are a result of super-solidus dislocation creep accompanied by dynamic recrystallization, creating neoblasts on grain boundaries between the larger grains, regardless of boundary orientation. There are also bimodal crystal size populations in the UZ leucogabbros and anorthosites, but there are key microstructural differences between these UZ samples and the dynamically recrystallized MZ sample, suggesting a different mode of super-solidus deformation. Critically, in contrast to the homogeneous spatial distribution expected for dynamic recrystallization, the UZ samples show a preferred distribution of the smaller grains on grain boundaries parallel to the plane of foliation (Fig. 3a–c; Fig. 4d, e; Fig. 7b, e). The small crystals often have a very different crystallographic orientation (misoriented by more than 60°) to their immediate larger neighbours, without the progressive change in orientation with increasing distance from the large grain that would be expected if the small crystals formed during dynamic recrystallization (Fig. 8b, d). Additionally, the small grains in the UZ samples are euhedral, in contrast to the rounded irregular shapes expected for dynamic recrystallization (Table 1, Fig. 3a–c, Fig. 4d–e). There is also a compositional difference between large and small plagioclase grains in the UZ, with the small crystals
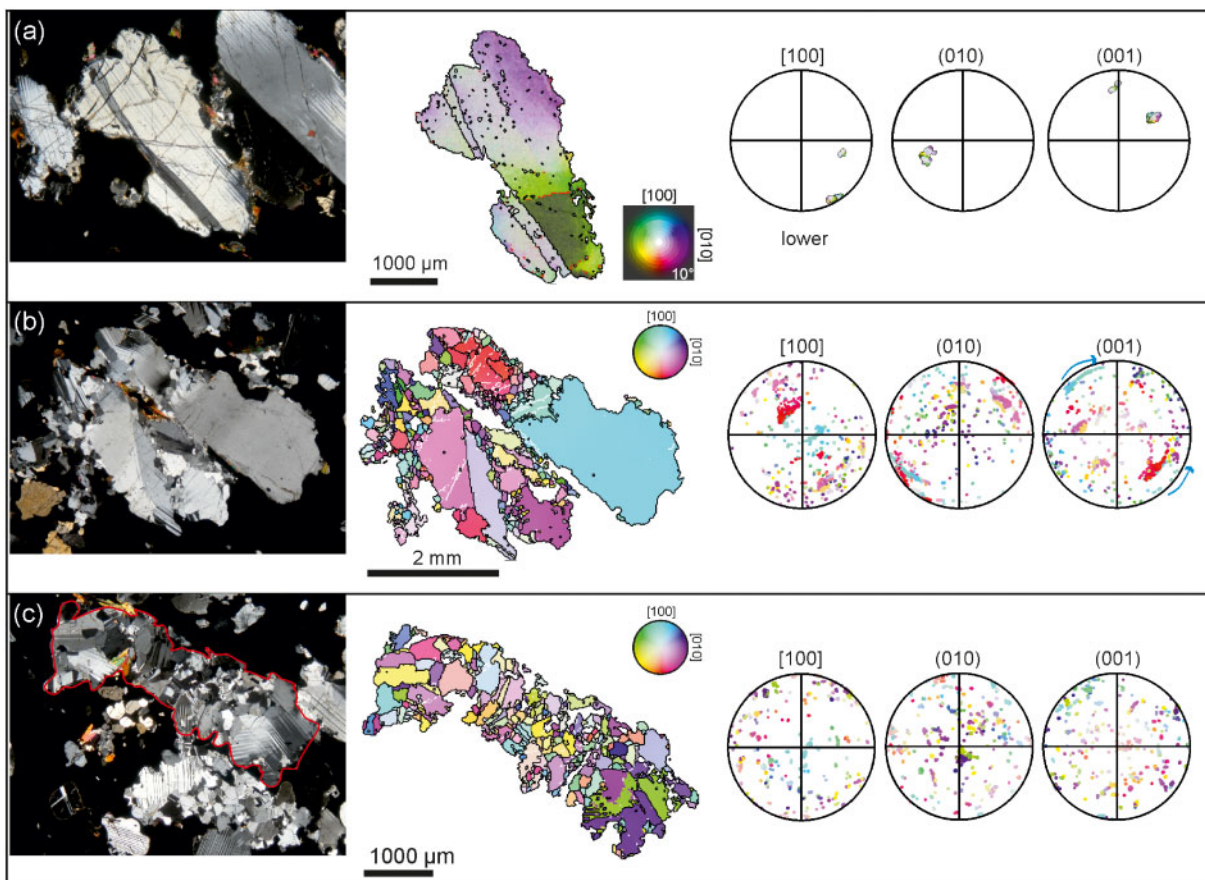
Fig. 10. Three types of plagioclase microstructure observed within magnetitite layers. (a) Photomicrograph, EBSD map and pole figure data for a single plagioclase crystal within the magnetitite layer. The EBSD map is coloured using the inverse pole figure (IPF) key referenced to the mean orientation of a grain. The colour scale is adjusted so that white represents 0° and black represents 10° of misorientation. Red lines on the EBSD map represent low-angle boundaries (<10°) and black lines are high-angle boundaries (>10°). (b) Photomicrograph, inverse pole figure orientation map, and pole figure data for plagioclase partially recrystallized along the grain boundaries. The teal arrow shows the dispersion of pole figures indicative of dislocation creep deformation. White lines on the EBSD map represent low-angle boundaries. (c) Photomicrograph, inverse pole figure orientation map and pole figure data for completely recrystallized plagioclase replacing original single euhedral laths. Pole figure data show that the grains within the recrystallized aggregate are randomly oriented.

typically less evolved (higher An#) than the larger grains (Fig. 11). We would not expect small grains to form during slow, uninterrupted, cooling of a partially solidified mush, since it is energetically more favourable for the interstitial liquid to form overgrowths on existing grains than to nucleate new ones (Vernon, 2004). We suggest instead that the small crystals in the UZ samples formed during an episode of enhanced undercooling related to deformation of the mush, triggering a burst of nucleation in the interstitial liquid. We term this process 'cavitation-driven nucleation'.

Deformation by diffusion creep is always accompanied by grain boundary sliding (Passchier & Trouw, 2005). Where deformation is sufficiently rapid to create an imbalance between grain boundary sliding and the necessary crystal plasticity or diffusional mass transport to accommodate it, micro-cavities open along grain boundaries. This process is called 'creep cavitation' (Kassner & Hayes, 2003; Dimanov *et al.*, 2007). Précigout & Stünitz, (2016) showed that olivine can nucleate in such micro-cavities during sub-solidus

deformation. We suggest that the rapid localised decompression accompanying creep cavitation in super-solidus crystal mushes may also create sufficient undercooling (i.e. departures from chemical equilibrium) to promote nucleation in the newly-formed cavities. Although the localised reduction in pore pressure associated with dilatation is strain-dependent (i.e. Reynolds dilatancy) and we might, therefore, expect only minor pore pressure reduction in slowly-deforming mushes in a regionally-subsiding magma chamber, John & Stünitz (1997) showed that fracturing parallel to foliation requires very small effective stress. The predominant localisation of the smaller plagioclase crystals parallel to the foliation defined by large plagioclase grains is consistent with this, suggesting that cavitation-driven nucleation was confined to cavities formed by separation of plagioclase grains within the foliation during deformation at low strain rates. The newly-formed plagioclase grains nucleated as a result of cavitation in a deforming mush are likely to be rotated into alignment with the shear direction, consistent with the
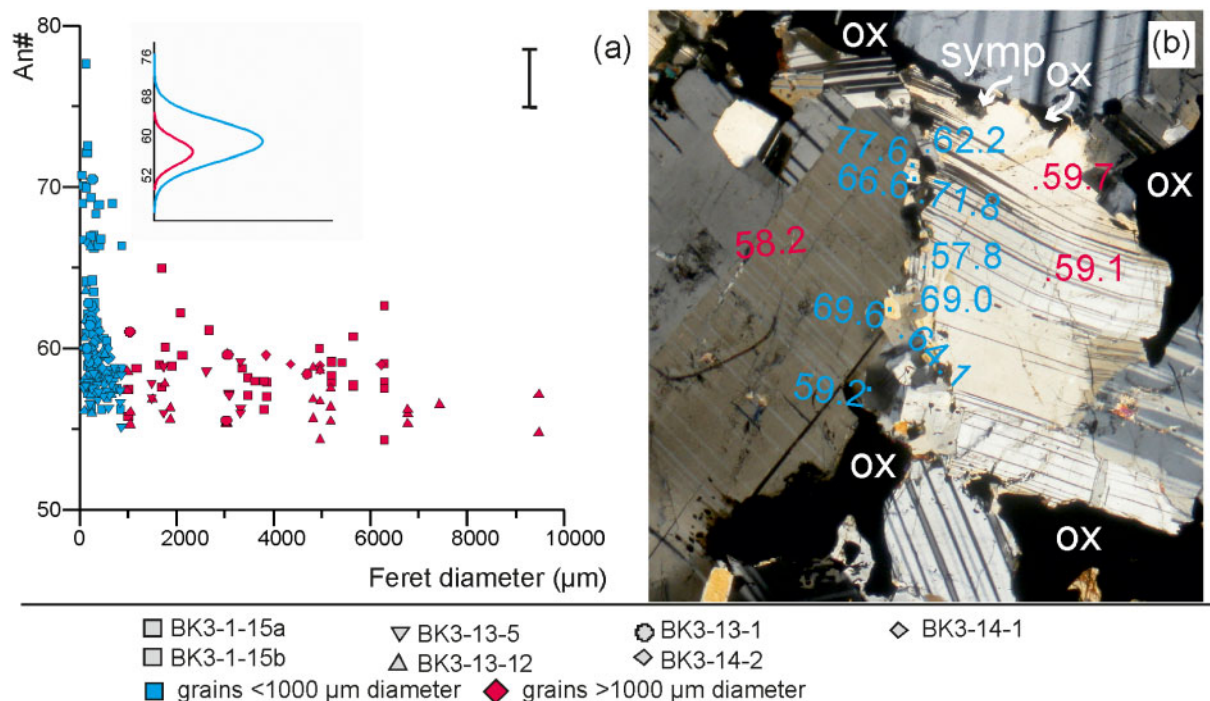
Fig. 11. (a) Feret diameter (the longest distance between any two points along the selection boundary measured by ImageJ) vs mol % anorthite. The inset in (a) is the normal distribution of An# for large (red) and small (blue) grains. (b) Plagioclase grains labelled with their composition (red for large grains and blue for small grains). Abbreviations: symp, symplectites; ox, magnetite. Detailed mineral chemical data are provided in Supplementary Data Table S3.

foliation and weak lineations recorded by the small plagioclase grains in our UZ magnetite layer (Fig. 8b; Table 2). The low aspect ratio of these small grains (Table 1) suggests that post-nucleation crystal growth occurred in a slow-cooling environment (Holness, 2014).

The driver for shearing of the UZ mush, in common with that of the MZ sample investigated here, is likely to be gravitational instability of the floor mush, perhaps induced by regional-scale deformation (e.g. Maier *et al.*, 2013). That we see significant differences in the microstructures formed during super-solidus, deformation of the MZ and UZ plagioclase-rich cumulates may be linked to differences in the amount of liquid present in the deforming mush (with higher liquid content in the UZ cumulates) or to differences in the strain rate during deformation.

The thickness of the plagioclase-rich mushy layer undergoing shearing in the UZ is not well-constrained, as the method of Holness *et al.* (2017a) only provides a precise measure of mush thickness at points in the stratigraphy where the liquidus assemblage changes. While the sharp lower boundaries of the magnetitite layers suggest that the Fe-rich liquid slurry flowed across an essentially rigid, low-permeability floor with a very thin mush, it is possible that a plagioclase-dominated mush may have reached several metres in thickness. Future work should focus on finding stratigraphic horizons containing both evidence of our newly-proposed cavitation-driven nucleation and field or microstructural evidence that can be used to precisely constrain mush thickness.

CONCLUSIONS

Despite a focussed examination of regions of the Bushveld stratigraphy containing mineralogical contrasts providing the greatest possible driver for internally-generated gravitationally-driven compaction of a crystal mush (i.e. thick, dense magnetitite layers), we found no convincing evidence that the deformation preserved in these rocks was a consequence of compaction. The thickest magnetitite layer we examined (113 cm) did not provide sufficient gravitational load to drive plastic deformation by dislocation creep, or to reduce the amount of interstitial liquid in the plagioclase-rich footwall compared to the hanging-wall. Instead, we suggest that the abundant evidence for super-solidus deformation in these rocks was a consequence of regional-scale events such as slumping and subsidence of the crystal mush.

Our microstructural examination of the UZ cumulates supports a history of mush mobility and a significant role of Fe-rich immiscible liquids in the formation of the magnetitite layers. Our microstructural observations of abundant fine-grained plagioclase grains in the UZ leucogabbros and anorthosites points to the possibility that shearing of a relatively liquid-rich crystal mush may drive crystal nucleation by localised undercooling within the cavities that form as the grains slide

past each other. This suggestion requires further detailed work (e.g. experiments and numerical modelling) to test this hypothesis and to place tight constraints on the relationship between strain rate, cavitation and localised departures from chemical equilibrium.

SUPPLEMENTARY DATA

Supplementary data are available at *Journal of Petrology* online.

REFERENCES

Ashwal, L. D., Webb, S. J. & Knoper, M. W. (2005). Magmatic stratigraphy in the Bushveld Northern Lobe: continuous geophysical and mineralogical data from the 2950 m Bellevue drillcore. *South African Journal of Geology* **108**, 199–232.

Bachmann, O. & Bergantz, G. W. (2004). On the origin of crystal-poor rhyolites: extracted from batholithic crystal mushes. *Journal of Petrology* **45**, 1565–1582.

Barnes, S.-J. & Maier, W. D. L. B. (2002). Platinum group element distributions in the Rustenburg Layered Suite of the Bushveld Complex, South Africa. In: Cabri, L.J. (ed.) *Canadian Institute of Mining Metallurgy and Petroleum Special Volume* **54**. Montreal, Canada: Canadian Institute of Mining, Metallurgy and Petroleum, pp. 483–506.

Bergantz, G. W., Schleicher, J. M. & Burgisser, A. (2017). On the kinematics and dynamics of crystal-rich systems. *Journal of Geophysical Research: Solid Earth* **122**, 6131–6159.

Boorman, S., Boudreau, A. & Kruger, F. J. (2004). The lower zone-critical zone transition of the bushveld complex: a quantitative textural study. *Journal of Petrology* **45**, 1209–1235.

Boudreau, A. E. & Meurer, W. P. (1999). Chromatographic separation of the platinum-group elements, gold, base metals and sulfur during degassing of a compacting and solidifying igneous crystal pile. *Contributions to Mineralogy and Petrology* **134**, 174–185.

Buick, I. S., Maas, R. & Gibson, R. (2001). Precise U-Pb titanite age constraints on the emplacement of the Bushveld Complex, South Africa. *Journal of the Geological Society* **158**, 3–6.

Cameron, E. N. (1976). Postcumulus and subsolidus equilibration of chromite and coexisting silicates in the eastern bushveld complex. In *Chromium: Its Physicochemical Behavior and Petrologic Significance*. Pergamon, pp. 1021–1033.

Carr, H. W. & Groves, D. I. (1994). The importance of synmagmatic deformation in the formation of Merensky Reef potholes in the Bushveld Complex. *Economic Geology* **89**, 1398–1410.

Cawthorn, R. G. (2015). The bushveld complex, South Africa. In: *Layered Intrusions*. Dordrecht: Springer, pp. 517–587.

Cawthorn, R. G., Barnes, S. J., Ballhaus, C. & Malich, K. N. (2005). Platinum group element, chromium and vanadium deposits in mafic and ultramafic rocks. *Economic Geology 100th Anniversary*, 215–249.

Cawthorn, R. G., De Wet, M., Hatton, C. J. & Cassidy, K. F. (1991a). Ti-rich chromite from the Mount Ayliff intrusion, Transkei: further evidence for high Ti tholeiitic magma. *American Mineralogist* **76**, 561–573.

Cawthorn, R. G., Meyer, P. S. & Kruger, F. J. (1991b). Major addition of magma at the Pyroxenite Marker in the Western Bushveld Complex, South Africa. *Journal of Petrology* **32**, 739–763.

Cawthorn, R. G. & Molyneux, T. G. (1986). Vanadiferous magnetite deposits of the Bushveld Complex. *Mineral deposits of Southern Africa. Geological Society of South Africa, Johannesburg* **2**, 1251–1266.

Dimanov, A., Rybacki, E., Wirth, R. & Dresen, G. (2007). Creep and strain-dependent microstructures of synthetic anorthite–diopside aggregates. *Journal of Structural Geology* **29**, 1049–1069.

Drury, M. R. & Urai, J. L. (1990). Deformation-related recrystallization processes. *Tectonophysics* **172**, 235–253.

Eales, H. V. & Cawthorn, R. G. (1996). The bushveld complex. In: Cawthorn, R. G. (ed.) *Layered Intrusions*. Amsterdam: Elsevier, pp. 181–230.

Engelbrecht, J. P. (1985). The chromites of the Bushveld Complex in the Nietverdiend area. *Economic Geology* **80**, 896–910.

Fischer, L. A., Wang, M., Charlier, B., Namur, O., Roberts, R. J., Veksler, I. V., Cawthorn, R. G. & Holtz, F. (2016). Immiscible iron-and silica-rich liquids in the Upper Zone of the Bushveld Complex. *Earth and Planetary Science Letters* **443**, 108–117.

Gerald, J. D. F. & Stünitz, H. (1993). Deformation of granitoids at low metamorphic grade. I: reactions and grain size reduction. *Tectonophysics* **221**, 269–297.

Hall, A. L. (1932). The bushveld igneous complex in central transvaal. *Geological Society of South Africa* **28**, 544.

Hielscher, R. & Schaeben, H. (2008). A novel pole figure inversion method: specification of the MTEX algorithm. *Journal of Applied Crystallography* **41**, 1024–1037.

Holness, M. B., Cawthorn, R. G. & Roberts, J. (2017a). The thickness of the crystal mush on the floor of the Bushveld magma chamber. *Contributions to Mineralogy and Petrology* **172**, 102.

Holness, M. B., Vukmanovic, Z. & Mariani, E. (2017b). Assessing the role of compaction in the formation of adcumulates: a microstructural perspective. *Journal of Petrology* **58**, 643–674.

Holness, M. B. (2014). The effect of crystallization time on plagioclase grain shape in dolerites. *Contributions to Mineralogy and Petrology* **168**, 1076.

Holness, M. B., Stripp, G., Humphreys, M. C. S., Veksler, I. V., Nielsen, T. F. & Tegner, C. (2010). Silicate liquid immiscibility within the crystal mush: late-stage magmatic microstructures in the Skaergaard intrusion, East Greenland. *Journal of Petrology* **52**, 175–222.

Humphreys, M. C. (2011). Silicate liquid immiscibility within the crystal mush: evidence from Ti in plagioclase from the Skaergaard intrusion. *Journal of Petrology* **52**, 147–174.

Hunter, R. H. (1996). Textural development in cumulate rocks. In: Cawthorn, R. G. (ed.) *Layered Intrusions*. Amsterdam: Elsevier, pp. 181–230.

Ji, S. & Mainprice, D. (1990). Recrystallization and fabric development in plagioclase. *The Journal of Geology* **98**, 65–79.

John, B. E. & Stünitz, H. (1997). Magmatic fracturing and small-scale melt segregation during pluton emplacement: evidence from the Adamello Massif (Italy). In: *Granite: From Segregation of Melt to Emplacement Fabrics*. Dordrecht: Springer, pp. 55–74.

Irvine, T. N. (1982). Terminology for layered intrusions. *Journal of Petrology* **23**, 127–162.

Kassner, M. E. & Hayes, T. A. (2003). Creep cavitation in metals. *International Journal of Plasticity* **19**, 1715–1748.

Kaufmann, F. E. D., Vukmanovic, Z., Holness, M. B. & Hecht, L. (2018). Orthopyroxene oikocrysts in the MG1 chromitite layer of the Bushveld Complex: implications for cumulate formation and recrystallization. *Contributions to Mineralogy and Petrology* **173**, 17.

Kruger, F. J., Cawthorn, R. G. & Walsh, K. L. (1987). Strontium isotope evidence against magma addition in the Upper Zone of the Bushveld Complex. *Earth and Planetary Science Letters* **84**, 51–58.

Kruse, R., Stünitz, H. & Kunze, K. (2001). Dynamic recrystallization processes in plagioclase porphyroclasts. *Journal of Structural Geology* **23**, 1781–1802.

Lafrance, B., John, B. E. & Frost, B. R. (1998). Ultra high-temperature and subsolidus shear zones: examples from the Poe Mountain anorthosite, Wyoming. *Journal of Structural Geology* **20**, 945–955.

Lafrance, B., John, B. E. & Scoates, J. S. (1996). Syn-emplacement recrystallization and deformation microstructures in the Poe Mountain anorthosite, Wyoming. *Contributions to Mineralogy and Petrology* **122**, 431–440.

Lee, J., Miller, M. M., Crippen, R., Hacker, B. & Vazquez, J. L. (1996). Middle Miocene extension in the gulf extensional province, Baja California - evidence from the Southern Sierra Juarez. *Journal Geological Society of America Bulletin* **108**, 505–525.

Maier, W. D., Barnes, S. J. & Groves, D. I. (2013). The Bushveld Complex, South Africa: formation of platinum–palladium, chrome- and vanadium-rich layers via hydrodynamic sorting of a mobilized cumulate slurry in a large, relatively slowly cooling, subsiding magma chamber. *Mineralium Deposita* **48**, 1–56.

Marsh, B. D. (1988). Crystal capture, sorting, and retention in convecting magma. *Geological Society of America Bulletin* **100**, 1720–1737.

Mathez, E. A., Hunter, R. H. & Kinzler, R. (1997). Petrologic evolution of partially molten cumulate - the atok section of the bushveld complex. *Contributions to Mineralogy and Petrology* **129**, 20–34.

McKenzie, D. (2011). Compaction and crystallization in magma chambers: towards a model of the skaergaard intrusion. *Journal of Petrology* **52**, 905–930.

Meurer, W. P. & Boudreau, A. E. (1998). Compaction of igneous cumulates part II: compaction and the development of igneous foliations. *The Journal of Geology* **106**, 293–304.

Meurer, W. P., Willmore, C. C. & Boudreau, A. E. (1999). Metal redistribution during fluid exsolution and migration in the Middle Banded series of the Stillwater Complex, Montana. *Lithos* **47**, 143–156.

Michels, Z. D., Tikoff, B., Kruckenberg, S. C. & Davis, J. R. (2015). Determining vorticity axes from grain-scale dispersion of crystallographic orientations. *Geology* **43**, 803–806.

Mitchell, A. A. (1996). Compositional cyclicity in a pyroxenitic layer from the Main Zone of the western Bushveld Complex: evidence for repeated magma influx. *Mineralogical Magazine* **60**, 149–161.

Morales, L. F. G., Boudier, F. & Nicolas, A. (2011). Microstructures and crystallographic preferred orientation of anorthosites from Oman ophiolite and the dynamics of melt lenses. *Tectonics* **30**, 1–21.

Namur, O., Abily, B., Boudreau, A. E., Blanchette, F., Bush, J. W. M., Ceuleneer, G., Charlier, B., Donaldson, C. H., Duchesne, J.-C. & Higgins, M. D. (2015). Igneous layering in basaltic magma chambers. In: *Layered Intrusions*. Dordrecht: Springer, pp. 75–152.

Passchier, C. W. & Trouw, R. A. J. (2005). *Microtectonics*. Germany: Springer.

Pebane, M. & Latypov, R. (2017). The significance of magmatic erosion for bifurcation of UG1 chromitite layers in the Bushveld Complex. *Ore Geology Reviews* **90**, 65.

Précigout, J. & Stünitz, H. (2016). Evidence of phase nucleation during olivine diffusion creep: a new perspective for mantle strain localisation. *Earth and Planetary Science Letters* **455**, 94–105.

Prior, D. J., Boyle, A. P., Brenker, F., Cheadle, M. C., Day, A., Lopez, G., Peruzzi, L., Potts, G., Reddy, S., Spiess, R., Timms, N. E., Trimby, P., Wheeler, J. & Zetterstrom, L. (1999). The application of electron backscatter diffraction and orientation contrast imaging in the SEM to textural problems in rocks. *American Mineralogist* **84**, 1741–1759.

Reddy, S. M. & Buchan, C. (2005). Constraining kinematic rotation axes in high-strain zones: a potential microstructural method? *Geological Society of London, Special Publications* **243**, 1–10.

Rybacki, E. & Dresen, G. (2004). Deformation mechanism maps for feldspar rocks. *Tectonophysics* **382**, 173–187.

Rosenberg, C. L. & Stünitz, H. (2003). Deformation and recrystallization of plagioclase along a temperature gradient: an example from the Bergell tonalite. *Journal of Structural Geology* **25**, 389–408.

Satsukawa, T., Ildefonse, B., Mainprice, D., Morales, L. F. G., Michibayashi, K. & Barou, F. (2013). A database of plagioclase crystal preferred orientations (CPO) and microstructures-implications for CPO origin, strength, symmetry and seismic anisotropy in gabbroic rocks. *Solid Earth* **4**, 511.

Scoon, R. N. & Mitchell, A. A. (2012). The Upper Zone of the Bushveld Complex at Roossenekal, South Africa: geochemical stratigraphy and evidence of multiple episodes of magma replenishment. *South African Journal of Geology* **115**, 515–534.

Skemer, P., Katayama, I., Jiang, Z. & Karato, S. (2005). The misorientation index: Development of a new method for calculating the strength of lattice-preferred orientation. *Tectonophysics* **411**, 157–167.

South African Committee for Stratigraphy & Geological Survey (South Africa) (1980). Lithostratigraphy of the republic of South Africa, South West Africa/Namibia, and the republics of Bophuthatswana, Transkei and Venda. Stratigraphy South Africa *Part 1.* Pretoria: South Africa. Republic of South Africa, Dept. of Mineral and Energy Affairs, Geological Survey.

Sparks, R. S. J., Huppert, H. E., Kerr, R. C., McKenzie, D. P. & Tait, S. R. (1985). Postcumulus processes in layered intrusions. *Geological Magazine* **122**, 555–568.

Stünitz, H. (1998). Syndeformational recrystallization – dynamic or compositionally induced? *Contributions to Mineralogy and Petrology* **131**, 219–236.

Svahnberg, H. & Piazolo, S. (2010). The initiation of strain localisation in plagioclase-rich rocks: Insights from detailed microstructural analyses. *Journal of Structural Geology* **32**, 1404–1416.

Tegner, C., Cawthorn, R. G. & Kruger, F. J. (2006). Cyclicity in the main and upper zones of the Bushveld Complex, South Africa: crystallization from a zoned magma sheet. *Journal of Petrology* **47**, 2257–2279.

Wallmach, T., Hatton, C. J. & Droop, G. T. R. (1985). Extreme facies of contact metamorphism developed in calc-silicate xenoliths in the eastern Bushveld Complex. *Canadian Mineralogist* **27**, 509–523.

Woods, A. W. & Stock, M. J. (2019). Some fluid mechanical constraints on crystallization and recharge within sills. *Philosophical Transactions of the Royal Society A: Mathematical, Physical and Engineering Sciences* **377**, 20180007.

VanTongeren, J. A., Hirth, G. & Kelemen, P. B. (2015). Constraints on the accretion of the gabbroic lower oceanic crust from plagioclase lattice preferred orientation in the Samail ophiolite. *Earth and Planetary Science Letters* **427**, 249–261.

VanTongeren, J. A. & Mathez, E. A. (2012). Large-scale liquid immiscibility at the top of the Bushveld Complex, South Africa. *Geology* **40**, 491–494.

VanTongeren, J. A. & Mathez, E. A. (2013). Incoming magma composition and style of recharge below the pyroxenite marker, eastern bushveld complex, South Africa. *Journal of Petrology* **54**, 1585–1605.

VanTongeren, J. A., Mathez, E. A. & Kelemen, P. B. (2010). A felsic end to Bushveld differentiation. *Journal of Petrology* **51**, 1891–1912.

Vernon, R. H. (1975). Deformation and recrystallization of a plagioclase grain. *American Mineralogist* **60**, 884–888.

Vernon, R. H. (2004). *A Practical Guide to Rock Microstructure*. Cambridge, UK: Cambridge University Press, 594 pp.

Von Gruenewaldt, G. (1973). The main and upper zones of the Bushveld Complex in the Roossenekal area, eastern Transvaal. *Transactions of the Geological Society of South Africa* **76**, 207–227.

Von Gruenewaldt, G. (1993). Ilmenite-apatite enrichments in the Upper Zone of the Bushveld Complex: a major titanium-rock phosphate resource. *International Geology Review* **35**, 987–1000.

Vukmanovic, Z., Barnes, S. J., Reddy, S. M., Godel, B. & Fiorentini, M. L. (2013). Morphology and microstructure of chromite crystals in chromitites from the Merensky Reef (Bushveld Complex, South Africa). *Contributions to Mineralogy and Petrology* **165**, 1031–1050.

Vukmanovic, Z., Fiorentini, M. L., Reddy, S. M. & Godel, B. (2018). Microstructural constraints on magma emplacement and sulfide transport mechanisms. *Lithosphere* **11**, 73–90.

Vukmanovic, Z., Holness, M. B., Monks, K. & Andersen, J. C. Ø. (2018). The Skaergaard trough layering: sedimentation in a convecting magma chamber. *Contributions to Mineralogy and Petrology* **173**, 1–18.

Wager, L. R. & Brown, G. M. (1968). *Layered Igneous Rocks*. Edinburgh and London: Oliver and Boyd, 588 pp.

Wenk, H.-R., Matthies, S., Donovan, J. & Chateigner, D. (1998). BEARTEX: a windows-based program system for quantitative texture analysis. *Journal of Applied Crystallography* **31**, 262–269.

White, S. (1975). Tectonic deformation and recrystallization of oligoclase. *Contributions to Mineralogy and Petrology* **50**, 287–304.

Williams, E., Boudreau, A. E., Boorman, S. & Kruger, F. J. (2006). Textures of orthopyroxenites from the Burgersfort bulge of the eastern Bushveld Complex, Republic of South Africa. *Contributions to Mineralogy and Petrology* **151**, 480–492.

Wilson, A. H. (2012). A chill sequence to the Bushveld Complex: insight into the first stage of emplacement and implications for the parental magmas. *Journal of Petrology* **53**, 1123–1168.

Wilson, A. H. (2015). The earliest stages of emplacement of the eastern Bushveld Complex: development of the Lower Zone, Marginal Zone and Basal Ultramafic Sequence. *Journal of Petrology* **56**, 347–388.

Yuan, Q., Namur, O., Fischer, L. A., Roberts, R. J., Lü, X. & Charlier, B. (2017). Pulses of plagioclase-laden magmas and stratigraphic evolution in the upper zone of the bushveld complex, South Africa. *Journal of Petrology* **58**, 1619–1643.

Zeh, A., Ovtcharova, M., Wilson, A. H. & Schaltegger, U. (2015). The Bushveld Complex was emplaced and cooled in less than one million years - results of zirconology, and geotectonic implications. *Earth and Planetary Research Letters* **418**, 103–114.